*International Journal of Microwave and Wireless Technologies*

**cambridge.org/mrf**

# Determining the nominal body contour image using wideband millimeter-wave radar for characterizing person-worn threats

Mohammad M. Tajdini and Carey M. Rappaport

Electrical and Computer Engineering Department, Northeastern University, 360 Huntington Ave., Boston, MA 02115, USA

**Research Paper**

**Cite this article:** Tajdini MM, Rappaport CM (2022). Determining the nominal body contour image using wideband millimeter-wave radar for characterizing person-worn threats. *International Journal of Microwave and Wireless Technologies* **14**, 732–738. https://doi.org/10.1017/S1759078721001276

Received: 27 February 2021
Revised: 28 July 2021
Accepted: 29 July 2021
First published online: 20 August 2021

**Key words:**
Computational imaging; millimeter-wave; remote sensing; inverse scattering; radar signal processing; Fourier reconstruction; counterterrorism

**Author for correspondence:**
Mohammad M. Tajdini,
E-mail: mmtajdini@gmail.com

## Abstract

Precise characterization of concealed person-worn objects will speed up the passenger screening process by reducing the rate of nuisance alarms, while also enhancing the airport security imaging systems. This paper presents an automatic, real-time method for wideband millimeter-wave radar identification of the nominal surface contours of the human body – even with affixed foreign objects or when a segment of the body cross-section is not captured by the radar – without relying on the body's bilateral symmetry. The developed method is verified experimentally when applied to the actual images generated by a laboratory airport scanning prototype developed recently by the US Department of Homeland Security (DHS). Our method uses the noisy collection of radar cross-section reflectivity data to extract the main contours and estimates the nominal body surface cross-sections through fitting a small-term Fourier series of circumferential variation. This is a necessary step for accurate characterizing of concealed terrorist threat objects affixed to the body.

## Introduction

More effective airport imaging system can ensure the safety of air travel while also minimizing the wait time in airport security lines. High-accuracy millimeter-wave (mm-wave) screening is an efficient solution to identify concealed terrorist threats or contraband, and is the primary full-body imaging technology used in airports by the US Transportation Security Administration (TSA) [1–3]. Mm-waves can readily pass through clothes but are reflected by the surface of the human body and by concealed objects [4–10]. Several innovative techniques have recently been proposed to improve the efficiency of mm-wave screening systems [6, 9–29]. In particular, Sheen and Hall developed more efficient reconstruction and calibration techniques to optimize the depth information [14]. Fernandes *et al.* investigated higher-order imaging artifacts of the current mm-wave security screening systems [15]. Yurduseven *et al.* proposed a fast simulation of full-size frequency-diverse aperture for imaging of human-scale targets [16]. Alvarez *et al.* demonstrated the feasibility of synthetic aperture radar screening to estimate the geometry and constitutive parameter information for low-permittivity lossless dielectric objects attached to flat and curved metallic plates [19–21]. Focused-beam continuous-wave radar was used for object characterization in security applications [23–25]. Passive mm-wave imaging techniques for the detection of concealed weapons attached to human body were elaborated in [26, 27]. Wang *et al.* discussed the advantages of active mm-wave imaging techniques [28]. The advantages of multistatic imaging configurations over monostatic systems, used currently in most airports, were illustrated by Nemati *et al.* [29].

Nuisance alarms from innocent objects are troublesome at airport checkpoints. Each nuisance alarm requires a secondary manual screening process in order to rule out the possibility of a concealed threat. While the mm-wave radar images demonstrate the features of threat objects clearly, they also show similar features of innocent objects. The precise characterization of detected objects will result in eliminating the need for pat downs in the case of innocent objects. Such characterization necessitates clear differentiation of nominal body surface contours from the concealed attached objects [19, 30] without relying on the body's bilateral symmetry; particularly in the case of naturally-occurring body asymmetries, or with symmetrically affixed foreign objects.

This paper presents a fully-automatic, real-time algorithm to estimate the nominal body surface contours by means of low-order Fourier modal reconstruction of the cross-section of the body part. Our developed technique relies on the observation that most human body cross-sections are smooth functions of circumferential angle $\varphi$ [31]. In contrast, an object affixed to the body would likely produce more rapid radial variation with respect to angle in the radar images. Mathematically, this implies that higher order terms of a Fourier series in $\varphi$ would be necessary in order to fit a contour with an affixed object than without. This

© The Author(s), 2021. Published by Cambridge University Press in association with the European Microwave Association

CAMBRIDGE UNIVERSITY PRESS

is essential for efficient approximation of the dielectric constant of the concealed affixed object and to rule out the innocent ones; leading to lower rates of nuisance alarm and the need for secondary pat downs. We experimentally verify our developed technique by applying it to the actual images of the High Definition-Advanced Imaging Technology (HD-AIT) system, a laboratory prototype for mm-wave airport screening developed recently by the DHS Science and Technology Directorate (S&T) [22, 32].

## Contour reconstruction from the measured reflectivity

Contour reconstruction of the human body via a noisy collection of 3D radar reflectivity is challenging. An automatic, real-time reconstruction algorithm for extracting the main contours is introduced through thresholding 2D cross-section slices of normalized reflectivity data into a 2D binary image. Pixels on the thick body-surface contour are assigned to unity, and the rest are assigned to zero. The width of contours is determined by the finite bandwidth of the radar. A Canny edge detector filter [33], via the MATLAB built-in function *edge*, applies a Gaussian filter, with the standard deviation of $\sqrt{2}$ and kernel size of 11×11, to decrease the image noise level, find the edges of the contour reflectivity, and remove the spurious output. The filter uses two thresholds to detect both strong and weak edges; thus, it is more resistant to the noise. The threshold values, typically from 0.06 for the lower threshold to 0.35 for the higher threshold, are different for topologically different body regions, but the same with or without the attached object. The goal is to accurately extract the nominal part of the body with no object attached, and use it to reconstruct the nominal body contour with affixed objects or shadowed by other body parts. The Canny edge detector filter parameters are selected empirically by applying the algorithm to a training dataset of reflectivity images, with and without the attached objects. The optimized parameters are further verified for a second testing dataset. Each dataset consists of reflectivity images from a variety of volunteers of different weights and genders wearing different clothing types and different numbers and types of concealed objects. The actual 3D images are generated by the HD-AIT screening system; a mm-wave laboratory prototype consists of a wide-bandwidth, circularly-polarized, multi-bistatic array of antennas working at 10–40 GHz with fine depth resolution and minimal attenuation through clothing [22, 32]. Opening and closing morphological operations are then used to remove small, isolated, or disconnected collections of pixels, and to unify the remaining pixels in the binary image [33]. More explicitly, the MATLAB built-in function *imclose* is used to expand parallel contours into one fat contour. Next, a second morphological operation is performed, via the MATLAB function *bwmorph*, to shrink each solid object with no hole into a minimally connected contour, and to reduce each object with a hole to a continuous ring midway between its outer boundary and the hole inside [34]. MATLAB functions *bwareaopen* and *imopen* are also used to remove features smaller than certain number of pixels, while the main axial contours are sharpened slice-by-slice. This further reduces the noise level of the radar image. The extracted contours can clearly indicate the position of foreign anomalies.

Figure 1 shows a projected image of the back view of a subject's legs captured by the HD-AIT system. There is a cylindrical 20 × 3 × 3 cm silicone rubber slab attached to the lower part of the left thigh. A 2D axial cross-section of the normalized reflectivity, with centroid object height $z = 0.62$ m, is shown in Fig. 2(a) for both left and right lower thighs, when the person faces to the direction shown by the arrow. Figure 2(b) depicts the effect of using the Canny edge detector filter, while Fig. 2(c) illustrates the result of applying morphological operations. Finally, Fig. 2(d) shows the clean, thin contour of the lower thighs. The depression in the left thigh is due to the affixed foreign object. The algorithm reduces the raw reflectivity data volume, lowers the noise level, includes object thickness information, and is performed fully automatically and in real-time.

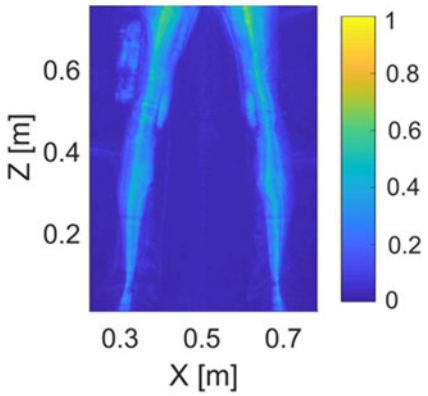



**Fig. 1.** Maximum intensity back view of an HD-AIT image of the legs. A cylindrical silicone rubber slab is attached to the lower part of the left thigh.

## Fourier approximation to determine the nominal contours of the body

The estimation of the human body surface contour is necessary for the characterization of the concealed affixed objects [19, 30]. We start from the observation that the radar reflectivity images of most parts of the human body are smoothly varying with respect to the circumferential angle $\varphi$. However, a foreign affixed object tends to appear in the reflectivity image as a discrete depression or protrusion with rapid radial variation with respect to the circumferential angle. This implies that a few-term Fourier series cannot fit the rapidly varying lumpiness due to the affixed object, but is enough to estimate the smoothly varying nominal body contour even in the presence of a foreign object attached to the body, or when sections of the body have not been fully captured by the multi-bistatic antennas of the screening system.

The Fourier approximation of a 2D nominal body contour is computed as follows: (1) Compute the centroid of the reconstructed contour and make it the center of the Cartesian coordinate system; (2) Transform the contour points from Cartesian to polar representation; (3) Calculate a few-term Fourier series with the amplitude coefficients $a_n$ and $b_n$, $n = 1, 2, \ldots, N$, through solving the following linear system of equations:

$$\begin{bmatrix} 1 & \cos(\varphi_1) & \ldots & \sin(N\varphi_1) \\ 1 & \cos(\varphi_2) & \ldots & \sin(N\varphi_2) \\ \vdots & \vdots & \vdots & \vdots \\ 1 & \cos(\varphi_M) & \ldots & \sin(N\varphi_M) \end{bmatrix} \begin{bmatrix} a_0 \\ a_1 \\ \vdots \\ b_N \end{bmatrix} = \begin{bmatrix} \rho_1 \\ \rho_2 \\ \vdots \\ \rho_M \end{bmatrix} \quad (1)$$

to fit best the extracted contour with $M$ points $(\varphi_m, \rho_m)$, $m = 1, 2, \ldots, M$, captured by the screening system; (4) Define an

https://doi.org/10.1017/S1759078721001276 Published online by Cambridge University Press

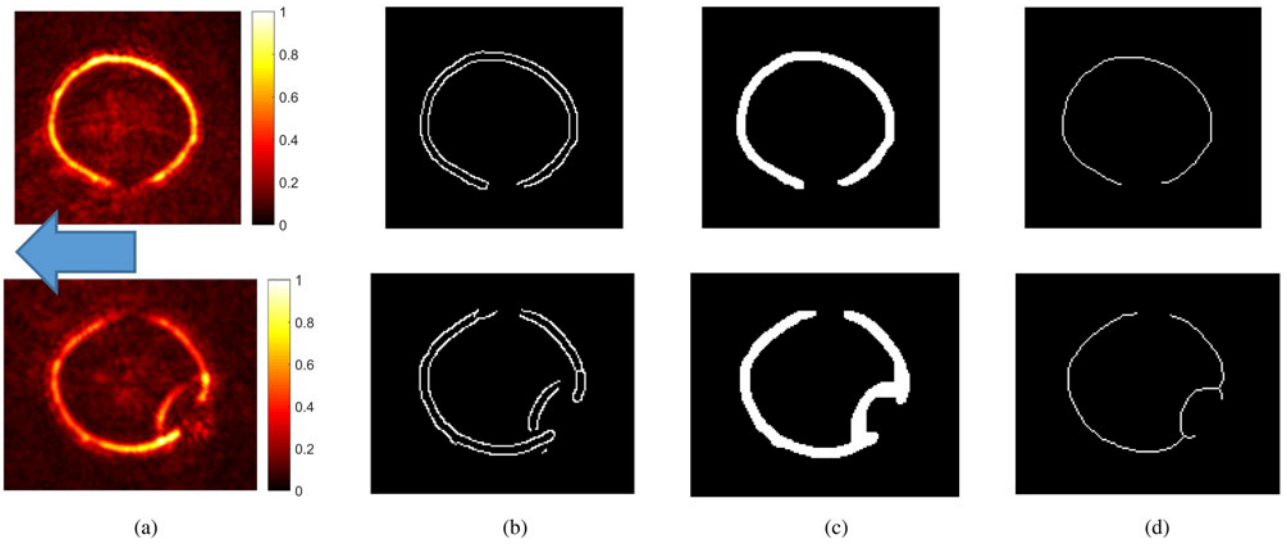



**Fig. 2.** Axial cross-sections of the lower part of the right thigh without the object (first row) and left thigh with the attached object (second row) of Fig. 1 both at $z$ = 0.62 m, when the subject faces to the left in the direction indicated by the arrow: (a) normalized reflectivity, (b) Canny edge detector filter output, (c) morphological processed output, and (d) the reconstructed contour. The depression in the second row of images is due to the affixed cylindrical silicone rubber slab.

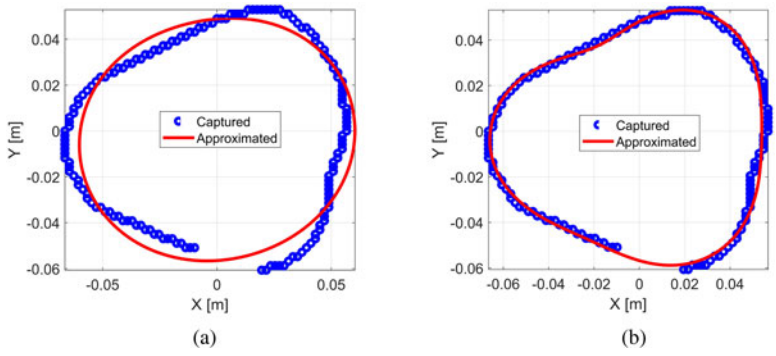



**Fig. 3.** (a) Five-term and (b) seven-term red Fourier series approximation to blue right knee contour points at $z$ = 0.47 m.

evenly-spaced array of $\varphi_i$ spanning from $-\pi$ to $+\pi$, and compute the 2D contour approximation

$$\rho(\varphi) = a_0 + \sum_{n=1}^{N} \{a_n \cos(n\varphi) + b_n \sin(n\varphi)\} \tag{2}$$

for every $\varphi_i$ even if the amplitude coefficients are not obtained from the entire $2\pi$ circumference, that is, sections of the reconstructed contour are absent from the image or within the object area; (5) Transform the approximated $\varphi - \rho$ points back to $x - y$ representation.

It is important that only the smooth variations of the extracted surface, with respect to the circumferential angle, be modeled as the nominal body contour. Therefore, the fewest number of terms is utilized for the Fourier modal series to model the nominal body surface. Our results indicate that five-term Fourier series ($N = 2$) is adequate to approximate human torso but is not enough for more challenging parts of the body. However, seven-term Fourier series ($N = 3$) is sufficient to approximate the nominal cross-sectional contours of more challenging regions of the body like knees and calves. As an example, a right knee cross-section at $z = 0.47$ m is shown in Fig. 3. While the five-term Fourier series cannot fit the predominantly triangular cross-section, the seven-term series approximates the entire contour well. The results can be compared quantitatively through computing the minimum distance of each contour point (blue) from the Fourier series approximation (red). While the root mean square error for the five-term series approximation is 0.49 cm, it is 0.15 cm when seven-term series is used. It is noted that when sections of the nominal body contour are not fully captured by the imaging system or are behind the attached foreign objects, the amplitude coefficients are found based on the remaining captured points alone. Any attached object, with faster angular variation relative to the low-order nominal body contour, will be classified as an anomaly (depression or protrusion in the images).

To show the effectiveness of the developed algorithm, the obtained contour of the lower part of the right thigh cross-section, as shown in the first row of Fig. 2, is examined. Although our contour extraction method correctly reconstructs the complete closed contour, we test the robustness of our Fourier series angular decomposition with artificially removing 1/6 of the contour, as shown in Fig. 4. The seven-term Fourier series fits the remaining blue contour points and estimates the missing green contour data. Figure 4(left) shows the calculated fit in $\varphi - \rho$ representation, and Fig. 4(right) illustrates the transformed fit in $x - y$ representation. Because of the slow

https://doi.org/10.1017/S1759078721001276 Published online by Cambridge University Press

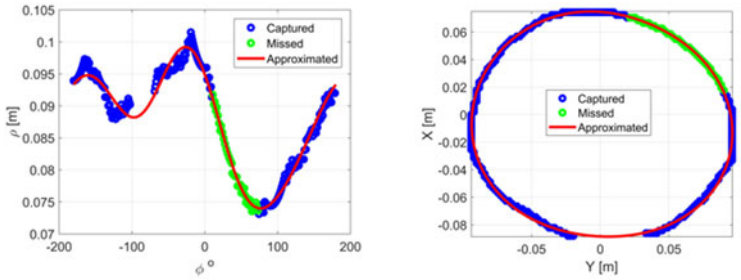



**Fig. 4.** Seven-term Fourier series fit to blue right thigh contour data of the first row of Fig. 2 in $\varphi-\rho$ representation (left) and $x-y$ representation (right). The result shows reasonable estimation of the full contour; even when 1/6 of the contour data (green) are artificially removed, in addition to a portion of missing contour data.

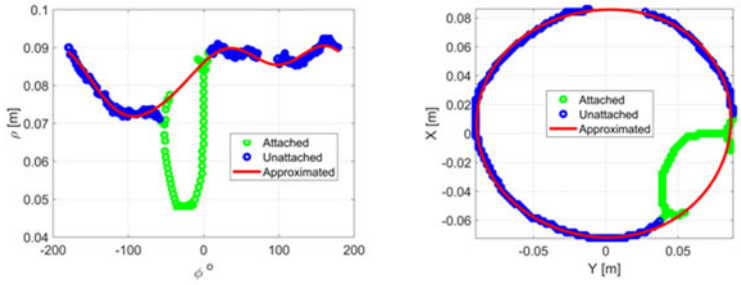



**Fig. 5.** Seven-term Fourier series fit to blue left thigh contour data of the second row of Fig. 2 in $\varphi-\rho$ representation (left) and $x-y$ representation (right). The result shows reasonable estimation of the full contour; even in the presence of the affixed silicone rubber slab (green), in addition to a portion of missing contour data. The reconstructed contour (red curve) approximates the nominal body surface for object characterization.

variation of radius as a function of circumferential angle, seven-term modal series is sufficient to accurately approximate the artificially removed portion of the contour. Our results show that the developed algorithm reconstructs the nominal body contour correctly if at least 2/3 of the consecutive data points on the nominal part of the main contour are extracted. For fewer consecutive data points, owing to a relatively large attached object size or an unexpected shadowing, the Fourier series result may diverge, which indicates the algorithm being unable to clear the anomaly. It will be up to the airport security officers to decide what to do with that information.

## Object characterization using Fourier modal approximation

The advantage of our developed Fourier angular series reconstruction for the characterization of attached objects is demonstrated via applying it to the actual images of the HD-AIT screening system for different types of objects. As the first example, we consider the extracted contour of the lower part of the left thigh cross-section, as shown in the second row of Fig. 2. The depression in the image is due to the presence of the affixed silicone rubber slab, with the estimated relative permittivity of $\varepsilon_r = 3$ [35]. The missing part is due to the shadowing by the right leg. Assuming the object region is given, based on the projected image of Fig. 1 by the automatic target recognition (ATR) (a software that all TSA scanners are currently equipped with) [36], the seven-term Fourier series approximation is employed to find the best fit by using all the remaining blue contour points; excluding the green depression points, as shown in Fig. 5. The seven-term Fourier series for a body cross-section is computed fully automatically and in real-time. Figure 5(left) shows the calculated fit in $\varphi-\rho$ representation, and Fig. 5(right) illustrates the transformed fit in $x-y$ representation. Next, the maximum displacement due to the depression (green) normal to the estimated nominal body contour via Fourier series fit (red) is calculated. The dielectric constant of the attached object is approximated as [19]

$$\sqrt{\varepsilon_r} \cong \left(1+\frac{d'}{d}\right)/\sqrt{p}, \tag{3}$$

where $d'$ is the displacement of the depressed contour from the nominal position (3.2 cm), $d$ is the thickness of the slab (3.0 cm), and $p$ is the correction factor for cylindrical cross-sections (1.1). The estimated dielectric constant will be 3.9, which is in good agreement with the 3.0 nominal value.

The next example is a $20 \times 3.5 \times 3.5$ cm cylindrical bag filled with liquid petroleum jelly attached to the upper left thigh between the legs at $z = 0.67$ m. The normalized reflectivity of a 2D cross-section is shown in Fig. 6(a). The main contour is extracted using the Canny edge detector filter and the morphological process, as depicted in Fig. 6(b). It is noted that the contour extraction alone cannot estimate the full contour, due to the low-intensity reflectivity. Figure 6(c) illustrates the derived Fourier series reconstruction result. It finds the best seven-term fit through using all the blue contour points, excluding the green depression region. With the displacement of the depressed contour from the nominal position ($d' = 1.9$ cm) and the thickness of the slab ($d = 3.5$ cm), the estimated dielectric constant will be 2.2, using Eq. (3). This is in perfect agreement with the 2.16 nominal value of petroleum jelly's relative permittivity [35].

Our Fourier series reconstruction of nominal body surface can be used not only to determine the electric permittivity of weak dielectric objects (seen as depressions in radar images) but also the thickness of highly conductive materials (seen as protrusions). As an example, an irregular metallic object of interest with the total size of $18 \times 12 \times 3$ cm attached to the front side of the subject's left calf at $z = 0.34$ m is shown in Fig. 7. The normalized reflectivity of a 2D cross-section is shown in Fig. 7(a). The reflectivity contour, extracted via using the Canny edge detector filter and the morphological process, is shown in Fig. 7(b). The result of seven-term Fourier series fit to blue contour points is depicted

https://doi.org/10.1017/S1759078721001276 Published online by Cambridge University Press

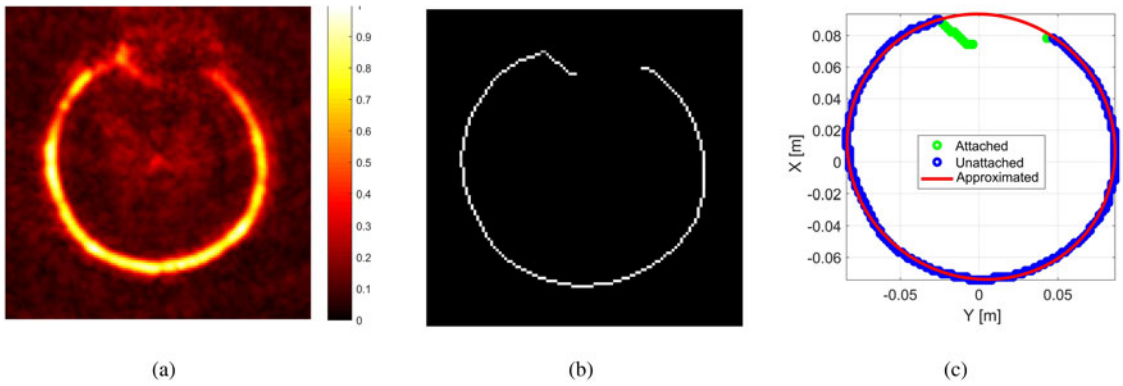



**Fig. 6.** (a) Normalized reflectivity of the 2D cross-section of a cylindrical bag filled with liquid petroleum jelly attached to the upper left thigh between the legs at $z = 0.67$ m, (b) the reconstructed contour using the Canny edge detector filter and morphological process, and (c) seven-term Fourier series fit to blue contour points. While the upper part of the image shows low-intensity reflectivity due to the presence of the foreign object, the reconstructed contour (red curve) approximates the nominal body surface for the characterization of the attached object.

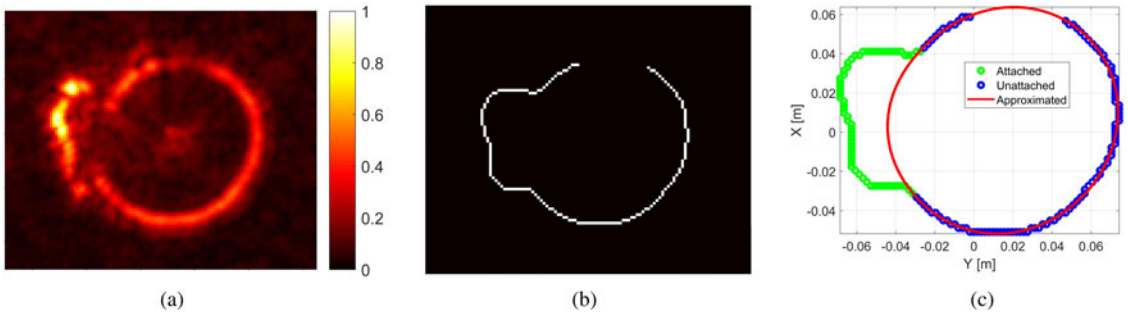



**Fig. 7.** (a) Normalized reflectivity of the 2D cross-section of an irregular metallic object of interest attached to the front side of the left calf at $z = 0.34$ m, (b) its reconstructed contour using the Canny edge detector filter and morphological process, and (c) seven-term Fourier series fit to blue contour points. About a quarter of the circumference is the object region (green points), while the upper part of the extracted contour is also missing. The reconstructed contour (red curve) approximates the nominal body surface for the entire circumference, and can be used to estimate the thickness of the attached object.

in Fig. 7(c). It is noted that about a quarter of the circumference is the object region (green points). Moreover, the upper part of the extracted contour is missing. The developed angular decomposition method is able to approximate the nominal body contour for the entire circumference. Comparing the maximum protrusion distance normal to the reconstructed nominal body contour, the estimated maximum thickness will be 2.7 cm; in excellent agreement with the 3.0 cm nominal value.

## Conclusion

The novelty of the proposed approach is in synthesizing several image processing techniques with Fourier circumferential decomposition method to estimate the nominal body contour under a penetrable dielectric or metallic foreign object that has similar characteristics to the potential, person-worn threats. It is performed automatically and in real-time for different body zones without relying on the body's bilateral symmetry. It shows promising results for the characterization of concealed foreign objects wrapped around or otherwise attached to the body. We validated the developed algorithm experimentally by applying it to the actual screening images of an HD-AIT system, a recently developed mm-wave laboratory prototype.

Based on the position and 2D projected extent of the detected object provided by the ATR system, and the 3D reflectivity images provided by the HD-AIT screening system, the algorithm identifies the body region where the affixed object presents and extracts the main contours for that topological region. Next, the Fourier modal decomposition method is applied, and the reconstructed nominal body contours are used for object characterization. The seven-term Fourier angular approximation fills in missing reflectivity data and highlights the regions of extracted contour with depression or protrusion. The flowchart of the algorithm is shown in Fig. 8. Assuming radar cross-section data are already available for deriving the cross-sections, the total computational time to calculate the reconstructed contour (including the time to load/save the input/output data) using MATLAB is 0.26 second per axial slice on a single-processor personal laptop with 2.2 GHz CPU and 6.0 GB RAM.

The reconstructed contour can be used to identify both the electric permittivity of weak dielectrics and thickness of both dielectric and metallic objects. This results in lowering the nuisance alarm rate in airport security checkpoints. While our Fourier fitting method is experimentally validated well for the actual images of the HD-AIT system, it is also important that the method is tested for other reference scanner experiments. That further testing ensures that the threshold parameters of the developed method are not too specifically tuned to the training dataset of the HD-AIT system. This task remains for future work.

https://doi.org/10.1017/S1759078721001276 Published online by Cambridge University Press

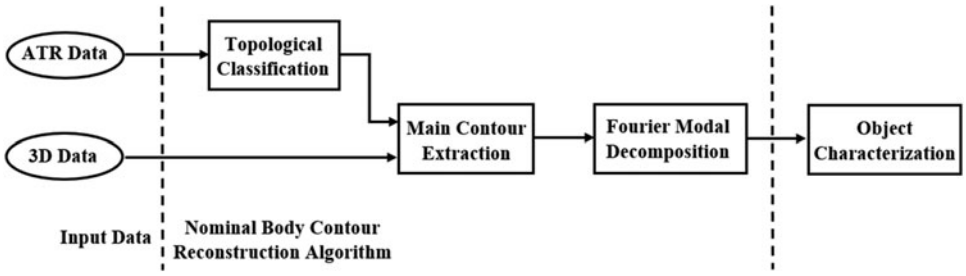



**Fig. 8.** The flowchart of the nominal body contour reconstruction algorithm.

**Acknowledgements.** This work is supported by the DHS S&T, under Grant Award 70RSAT18FR0000115. The views and conclusions contained herein are those of the authors and should not be interpreted as necessarily representing the official policies, either expressed or implied, of DHS. The authors would like to thank the reviewers for their constructive comments. They are also grateful to Prof. Jose A. Martinez-Lorenzo and Kurt P. Jaisle for their helpful discussions.

## References

1. **Moulder JE** (2012) Risks of exposure to ionizing and millimeter-wave radiation from airport whole-body scanners. *Radiation Research* **177**, 723–726.
2. **Passive Millimeter Wave Detectors Market Survey Report, DHS S&T, SAVER Prog., (2014).**
3. **Laviada J, Lopez-Portugues M, Arboleya-Arboleya A and Las-Heras F** (2018) Multiview mm-wave imaging with augmented depth camera information. *IEEE Access* **6**, 16869–16877.
4. **Alekseev S and Ziskin M** (2007) Human skin permittivity determined by millimeter wave reflection measurements. *Bioelectromagnetics* **28**, 331–339.
5. **Bjarnason J, Chan T, Lee A, Celis M and Brown E** (2004) Millimeter-wave, terahertz, and mid-infrared transmission through common clothing. *Applied Physics Letters* **85**, 519–521.
6. **Sheen DM** (2015) Noise analysis for near field 3-D FM-CW radar imaging systems. *Proceedings of SPIE* **946206**, 9462061–9462067.
7. **Accardo J and Chaudhry MA** (2014) Radiation exposure and privacy concerns surrounding full-body scanners in airports. *Journal of Radiation Research and Applied Sciences* **7**, 198–200.
8. **Appleby R and Wallace HB** (2007) Standoff detection of weapons and contraband in the 100 GHz to 1 THz region. *IEEE Transactions on Antennas and Propagation* **55**, 2944–2956.
9. **Sheen DM, McMakin DL and Hall TE** (2010) Near-field three-dimensional radar imaging techniques and applications. *Applied Optics* **49**, E83–E93.
10. **Sheen DM, Bernacki BE and McMakin DL** (2012) Advanced millimeter-wave security portal imaging techniques. *Proceedings of SPIE* **8259**, 82590G1–82590G7.
11. **Alvarez Y, Gonzalez-Valdes B, Martinez-Lorenzo JA, Las-Heras F and Rappaport CM** (2013) An improved SAR based technique for accurate profile reconstruction. *IEEE Transactions on Antennas and Propagation* **61**, 1490–1495.
12. **Sheen DM, McMakin DL, Hall TE and Severtsen RH** (2009) Active millimeter-wave standoff and portal imaging techniques for personnel screening. *IEEE Conference on Technologies for Homeland Security*, Boston, MA, pp. 440–447.
13. **Sheen DM, McMakin DL and Hall TE** (2011) Active millimeter-wave and sub-millimeter-wave imaging for security applications. *International Conference on Infrared, Millimeter, and Terahertz Waves*, Houston, TX, pp. 2–7.
14. **Sheen DM and Hall TE** (2011) Calibration, reconstruction, and rendering of cylindrical millimeter-wave image data. *Proceedings of SPIE* **8022**, 8022H1–8022H12.
15. **Fernandes JL, Rappaport CM and Sheen DM** (2011) Improved reconstruction and sensing techniques for personnel screening in three-dimensional cylindrical millimeter-wave portal scanning. *Proceedings of SPIE* **8022**, 8022051–8022058.
16. **Yurduseven O, Gollub JN, Rose A, Marks DL and Smith DR** (2016) Design and simulation of a frequency-diverse aperture for imaging of human-scale targets. *IEEE Access* **4**, 5436–5451.
17. **Fromenteze T, Yurduseven O, Berland F, Decroze C, Smith DR and Yarovoy AG** (2019) A transverse spectrum deconvolution technique for MIMO short-range Fourier imaging. *IEEE Transactions on Geoscience and Remote Sensing* **57**, 6311–6324.
18. **Marks DL, Yurduseven O and Smith DR** (2017) Fourier accelerated multistatic imaging: a fast reconstruction algorithm for multiple-input-multiple-output radar imaging. *IEEE Access* **5**, 1796–1809.
19. **Gonzalez-Valdes B, Alvarez Y, Martinez-Lorenzo JA, Las-Heras F and Rappaport CM** (2013) SAR processing for profile reconstruction and characterization of dielectric objects on the human body surface. *Progress in Electromagnetics Research* **138**, 269–282.
20. **Alvarez Y, Gonzalez-Valdes B, Martinez-Lorenzo JA, Las-Heras F and Rappaport CM** (2012) 3D whole body imaging for detecting explosive-related threats. *IEEE Transactions on Antennas and Propagation* **60**, 4453–4458.
21. **Alvarez Y, Gonzalez-Valdes B, Martinez-Lorenzo JA, Las-Heras F and Rappaport CM** (2015) SAR imaging-based techniques for low permittivity lossless dielectric bodies characterization. *IEEE Antennas and Propagation Magazine* **57**, 267–276.
22. **Sheen DM, Fernandes JL, Tedeschi JR, McMakin DL, Jones AM, Lechelt WM and Severtsen RH** (2013) Wide-bandwidth, wide-beamwidth, high-resolution, millimeter-wave imaging for concealed weapon detection. *Proceedings of SPIE* **8715**, 8715091–87150911.
23. **Sadeghi M, Wig E and Rappaport C** (2018) Determining the dielectric permittivity and thickness of a penetrable slab affixed to the human body using focused CW mm-wave sensing. *2018 IEEE International Symposium on Antennas and Propagation and USNC/URSI National Radio Science Meeting*, pp. 621–622.
24. **Tajdini MM and Rappaport CM** (2019) Focused CW mm-wave characterization of lossy penetrable dielectric slab affixed to human body. *2019 IEEE International Symposium on Antennas and Propagation and USNC-URSI Radio Science Meeting*, pp. 577–578.
25. **Sadeghi M, Tajdini MM, Wig E and Rappaport CM** (2020) Single-frequency fast dielectric characterization of concealed body-worn explosive threats. *IEEE Transactions on Antennas and Propagation* **68**, 7541–7548.
26. **Appleby R and Anderton RN** (2007) Millimeter-wave and submillimeter-wave imaging for security and surveillance. *Proceedings of the IEEE* **95**, 1683–1690.
27. **Zheng C, Yao X, Hu A and Miao J** (2013) A passive millimeter-wave imager used for concealed weapon detection. *PIER B* **46**, 379–397.
28. **Wang Z, Chang T and Cui HL** (2019) Review of active millimeter wave imaging techniques for personnel security screening. *IEEE Access* **7**, 148336–148350.
29. **Nemati MH, Mantzavinos S, Busuioc D, Pelepchan N, Brevett T, Londa J, Phatak N, Castle D and Rappaport CM** (2018) Experimental validation of a novel multistatic toroidal reflector nearfield imaging system for

https://doi.org/10.1017/S1759078721001276 Published online by Cambridge University Press

concealed threat detection. *12th European Conference on Antennas and Propagation (EuCAP)*, pp. 1–3.
30. **Asri M and Rappaport C** (2019) Automatic permittivity characterization of a weak dielectric attached to human body using wideband radar image processing. *IEEE International Symposium on Antennas and Propagation*, Atlanta, GA, pp. 575–576.
31. **Tajdini MM, Jaisle KP and Rappaport CM** (2020) Image radar determining the nominal body contour for characterization of concealed person-worn explosives. *14th European Conference on Antennas and Propagation (EuCAP)*, Copenhagen, Denmark, pp. 1–4.
32. *Passenger Screening Algorithm Challenge*, Department of Homeland Security. [Online]. Available: https://www.kaggle.com/c/passenger-screening-algorithm-challenge/data.
33. **Gonzalez RC and Woods RE** (2018) *Digital Image Processing*, 4th Edn. New York, NY: Pearson.
34. Morphological operations on binary images, MathWorks. [Online]. Available: https://www.mathworks.com/help/images/ref/bwmorph.html.
35. **Von Hippel R** (1953) *Dielectric Materials and Applications*. New York, NY: Technology Press of MIT and John Wiley and Sons, Inc.
36. *Passenger Screening Using Advanced Imaging Technology*, US Department of Homeland Security, Federal Register, **81**(42), 2016.



**Mohammad M. Tajdini** received the Ph.D. degree in electrical engineering from Northeastern University, Boston, MA, USA, in 2016, with a focus on radar detection of buried threat objects. From 2016 to 2017, he was a Post-Doctoral Research Fellow with the School of Medicine, University of Maryland, Baltimore, MD, USA, where he was involved in imaging of lung cancer tumors. Since 2017, he has been a Post-Doctoral Research Associate with Northeastern University, working on the detection of suicide bomber explosives. He is also a Lecturer with the College of Engineering, Northeastern University. His research interests include electromagnetic modeling, sensing, and imaging.



**Carey M. Rappaport** (Fellow, IEEE) received the SB degree in mathematics and the SB, SM, and EE degrees in electrical engineering from the Massachusetts Institute of Technology (MIT), Cambridge, MA, USA, in 1982, and the Ph.D. degree in electrical engineering from MIT, in June 1987. He joined the ECE Faculty of Northeastern University, Boston, MA, USA, in 1987. In 2011, he was appointed COE Distinguished Professor. During fall 1995, he was a Fulbright Scholar Visiting Professor with the Electromagnetics Institute of the Technical University of Denmark, Lyngby. In 2005, he was a Visiting Research Scientist with CSIRO in Epping, Australia. He was PI of an ARO-sponsored MURI in Humanitarian Demining, Co-PI of the NSF-sponsored CenSSIS Engineering Research Center, and Co-Pl of the DHS ALERT Center of Excellence. He has authored over 430 technical journal and conference papers in the antenna design, wave propagation and scattering computation, and bioelectromagnetics.

https://doi.org/10.1017/S1759078721001276 Published online by Cambridge University Press